Changes in global vegetation activity and its driving factors during 1982-2013

Running head: Changes in vegetation and driving factors

Lin Zhao[1], Aiguo Dai[2*], Bo Dong[2]

[1] School of Resource and Environmental Sciences, Wuhan University, Wuhan, Hubei, China

[2] Department of Atmospheric and Environmental Sciences, University at Albany, State University of New York, Albany, NY, USA

*Correspondence: Dr. Aiguo Dai, Department of Atmospheric and Environmental Sciences, University at Albany, SUNY, Albany, New York 12222, USA; Tele.: 518-442-4474, Fax: 518-442-4474, e-mail: adai@albany.edu

Keywords: NDVI, vegetation activity, climatic oscillation, external forcing, trend attribution

Type of Paper: Primary research article

© 2017. This manuscript version is made available under the Elsevier user license
http://www.elsevier.com/open-access/userlicense/1.0/

Abstract

Vegetation activity plays a crucial role in the global carbon cycle and climate. Many studies have examined recent changes in vegetation growth and the associated local climatic drivers. They revealed a global greening trend during the recent decades. However, few studies have analyzed how remote oceanic conditions affect land vegetation growth through atmospheric teleconnection, and the causes of the recent greening needs further investigation. In this study, we investigate the spatio-temporal variations (including trends) of vegetation activity using satellite data of growing-season normalized difference vegetation index ($NDVI_{gs}$), and examine their relationship to local and remote climate oscillations and external anthropogenic forcing by statistical means. As expected, there is an increasing trend in global-mean $NDVI_{gs}$ from 1982-2013, with significant greening over Europe and many other land areas. $NDVI_{gs}$ is temperature-limited at northern high-latitudes, but water-limited in arid and semi-arid regions, and radiation-limited in the Amazon and eastern and southern Asia. Globally, El Niño-Southern Oscillation (ENSO) is the leading climatic driver of interannual variability of $NDVI_{gs}$, especially over southern and eastern Africa, eastern Australia, northeastern Asia, and northern South America. Consistent with previous modeling studies, a regression-based attribution analysis suggests that historical anthropogenic forcing (mainly increases in greenhouse gases) explains about two thirds of the $NDVI_{gs}$ trend from 1982-2013, with the rest coming mainly from the Atlantic Multi-decadal Oscillation (AMO). Contributions to the recent $NDVI_{gs}$ trend from ENSO and Pacific decadal variability and Artctic Oscillation appear to be small.

1. Introduction

Vegetation is the main component of the terrestrial ecosystem and it plays a critical role in global carbon, water and energy cycles. Under global warming, how plant's photosynthesis responds to warmer temperature and other extreme events, such as frequent and prolonged droughts (Dai, 2011a, 2011b; Dai, 2013; Trenberth et al., 2014; Dai and Zhao, 2017), has become increasingly important for understanding the impact of climate change on terrestrial carbon fluxes and thus atmospheric CO_2 concentrations.

Many studies have showed that global vegetation activities have changed during the last several decades over various climate zones, vegetation types, and soil types. These changes include the greening in Europe (Zhou et al., 2001; Julien et al., 2006), the eastern U.S. (Xiao and Moody, 2005), China (Peng et al., 2011; Xu et al., 2014), India (De Jong et al., 2012), the Sahel (Anyamba and Tucker, 2005; Olsson et al., 2005), and western and southern Australia (Ukkola et al., 2015); and the browning over southern Africa (Ichii et al., 2002), southern South America (Xiao and Moody, 2005), northern North America (De Jong et al., 2013) and Southeast Asia (Zhang et al., 2016). These vegetation changes can affect the air-land carbon exchange. During the 1980s and 1990s, the global terrestrial ecosystems were a net carbon sink (Dai and Fung, 1993; Schimel et al., 2001). From 2000 to 2009, however, vegetation productivity declined over large parts of the Southern Hemisphere (SH), which offset the greening in the Northern Hemisphere (NH) and resulted in a reduction in global productivity (Zhao and Running, 2010; Piao et al., 2011).

Based mainly on statistical analyses, previous studies have also examined local climate drivers for vegetation change. The three leading climatic drivers are precipitation, temperature and radiation, which act as the limiting factor for 52%, 31%, and 5% of global vegetated areas, respectively (Churkina and Running et al., 1998). Their effects vary across climate zones, ecosystem types, biomes and plant species. Temperature dominates vegetation growth in northern high-latitudes (Churkina and Running et al., 1998; Zhou et al., 2001; Nemani et al., 2003; Xiao and Moody, 2005; Piao et al., 2014), while precipitation dominates in arid and semiarid areas (Kawabata et al., 2001; Nemani et al., 2003; Hickler et al., 2005; Fensholt et al., 2012), with radiation as the limiting factor only in tropical rainforests (Nemani et al., 2003; Schuur 2003). Drought, manifested as both water deficit and high temperatures, was found to limit vegetation growth in the Amazon (Phillips et al., 2009; Doughty et al., 2015), North America (Ji and Peters, 2003; Quiring and Ganesh, 2010), Europe (Ciais et al., 2005; Pasho et al., 2011), Congo rainforests (Zhou et al., 2014), and other regions (Vicente-Serrano et al., 2013).

Most previous studies have focused on the relationship between vegetation and local climatic factors. Few studies have examined the teleconnection of local vegetation growth to remote oceanic conditions. However, many studies have shown that natural climate oscillations, such as the El Niño-Southern Oscillation (ENSO), the Pacific Decadal Oscillation (PDO) or the Inter-decadal Pacific Oscillation (IPO), the Arctic Oscillation (AO), and the Atlantic Multi-decadal Oscillation (AMO) (Liu, 2012) can have large impacts on temperature and precipitation over many remote land areas (e.g., Ropelewski and Halpert, 1989; Thompson and Wallace, 1998; Dai and Wigley, 2000; Buermann et al., 2003; Dai, 2013; Gu and Adler, 2013, 2015; Dong and Dai, 2015). Thus, natural climate variations originated from the oceans could contribute to recent variations and changes in terrestrial vegetation activity through their influences on climate fields. Philippon et al. (2014) have highlighted the impact of ENSO on vegetation dynamics in Africa through its influences on rainfall, solar radiation, and temperature. El Niño events were found to be associated with the negative NDVI anomaly in central India (Bothale and Katpatal, 2014) and northeastern Brazil (Erasmi et al., 2014). Previous studies also found that ENSO and AO were the principal drivers of interannual variability in NH greenness during 1982-1998 (Buermann et al., 2003), while PDO and AMO could explain about half of NH NDVI variations during 2000-2015 (Bastos et al., 2017). In general, warm ENSO and PDO/IPO events are associated with decreased greenness in Australia, Southeast Asia, northeastern South America and southern Africa, but increased greenness in eastern Africa, central Asia, and northern North America (Woodward et al., 2008; Miralles et al., 2014).

A few studies have focused on attribution of recent greening trends through model simulations. Although limited by modeling uncertainties, these studies suggest that CO_2 fertilization is the dominant contributor to the recent global trend in NDVI (Los, 2013) and leaf area index (LAI) (Mao et al., 2013; Zhu et al., 2016), followed by climate change, nitrogen deposition and other factors (Zhu et al., 2016). Mao et al. (2016) have gone a further step to attribute the greening of the northern extratropical land surface to anthropogenic forcing, primarily human-produced greenhouse gases (GHGs).

This study aims to investigate the variations and changes of global vegetation activity from 1982-2013 using the NDVI dataset from the Global Inventory Monitoring and Modeling Systems (GIMMS) (Tucker et al., 2005), and examine the relationship between NDVI and local climate factors and remote climatic oscillations. Another focus is on the attribution of the recent global NDVI trends and variations to external anthropogenic forcings (such as increases in

GHGs) and internal modes of climate variability (such as ENSO, AO and AMO). This study differs from the previous studies by making an extra step to explain the variations and changes in global vegetation growth in terms of internal climate modes of variability (mainly of oceanic origin) as well as external climate forcing. The results should improve our understanding of the underlying drivers of recent changes in global terrestrial vegetation activity based on observational analyses, in contrast to previous modeling studies.

2. Data and methods

2.1. NDVI data

To quantify vegetation activity, we used the latest GIMMS3g NDVI dataset (http://ecocast.arc.nasa.gov/) derived from the Advanced Very High-resolution Radiometer (AVHRR) on satellites operated by the National Oceanographic and Atmospheric Administration (NOAA) (Tucker et al., 2005). It spans from January 1982 through December 2013 on a 1/12 degree grid and is available twice a month. This study focuses on the vegetation activity in the growing season, which is defined here as April-October for 20°N-70°N, October-April for 20°S-60°S, and January-December (i.e., the whole year) for 20°S-20°N. We first calculated the time series of NDVI for growing season ($NDVI_{gs}$) over each 1/12 degree pixel with NDVI > 0 during the growing seasons. To match with climate data, the raw $NDVI_{gs}$ data were simply averaged onto a 2.5°×2.5° grid. Additionally, areas with very sparse vegetation cover (long-term mean $NDVI_{gs} < 0.1$) were masked out as well as the Arctic regions (north of 70°N). Time series of the global (60°S-70°N) mean $NDVI_{gs}$ from 1982-2013 were obtained by averaging over all the pixels with $NDVI_{gs} \geq 0.1$ using area as the weighting.

2.2. Climate data

Observational data for monthly surface air temperature (T) over land were obtained from the Climate Research Unit (CRU) at the University of East Anglia (TS3.22; Harris et al., 2014). The CRU TS 3.22 dataset covers 1901-2014 on a 0.5° grid and was derived by interpolating T anomalies from ~4000 weather stations (Mitchell and Jones, 2005). The CRU monthly temperature data were simply averaged onto the 2.5° grid.

Monthly precipitation (P) data were obtained from Global Precipitation Climatology Centre (GPCC) v7 dataset, which covers 1901-2010 (Schneider et al., 2014). The Global Precipitation Climatology Project (GPCP) v2.2 (Huffman et al., 2009) data for 2011-2013 were used to extend the P series to 2013. Before merging, the two datasets were adjusted to have the same mean over a common period (1981-2010) at each grid box on a 2.5^{o} grid.

Monthly data of sea surface temperatures (SSTs) were obtained from the Hadley Centre Sea Ice and Sea Surface Temperature dataset (HadISST) (Rayner et al., 2003), which was derived from *in-situ* observations and covers our study period (1982-2013) with a spatial resolution of 1°×1°.

Monthly data for photosynthetically active radiation (PAR) were from the NASA/Global Energy and Water Cycle Experiment (GEWEX) Surface Radiation Budget (SRB3.0) dataset, which were obtained from the NASA Langley Research Center Atmospheric Science Data Center (https://eosweb.larc.nasa.gov). The PAR data were generated using an updated version of the University of Maryland's shortwave and longwave flux algorithm and the International Satellite Cloud Climatology Project (ISCCP) DX radiance and cloud parameters (Rossow and Schiffer, 1999). The PAR dataset only covers 1984-2007 on a 1°×1° grid, which was first assigned onto a 0.5^{o} grid and then averaged onto the 2.5° grid.

We used the monthly self-calibrated Palmer Drought Severity Index with Penman-Monteith potential evapotranspiration (sc_PDSI_pm) produced by Dai et al. (Dai et al., 2004; Dai, 2011a, 2011b, 2013; Dai and Zhao 2017) as a measure of surface aridity. The sc_PDSI_pm was calculated using historical meteorological data on the 2.5° grid for 1850-present and is available from http://www.cgd.ucar.edu/cas/catalog/climind/pdsi.html.

We used indices for ENSO and IPO (ENSO&IPO thereafter, Dong and Dai 2015), AMO (Liu, 2012), and AO (Thompson and Wallace, 1998) to represent the leading modes of climate variability originated from the tropical Pacific Ocean, the North Atlantic Ocean, and the northern mid-high latitude atmosphere, respectively. We chose these climate modes because they are the most studied, well-known oscillations that have significant impacts on global climate. ENSO is the dominant mode of interannual (2-7 year) variations in sea surface temperatures (SSTs) and winds over the tropical Pacific Ocean, which can influence weather and climate in many regions of the world through atmospheric teleconnections (Ropelewski and Halpert, 1989; Dai and Wigley, 2000). The PDO and IPO refer to the decadal to multi-decadal variations in Pacific SSTs. Both of them have essentially the same SST anomaly patterns that are ENSO-like (Zhang et al., 1997), with PDO focusing more on the North Pacific domain while IPO covering the whole Pacific (Dong and Dai 2015). The AMO is a climate mode of 60-80 years oscilation seen in North Atlantic SSTs. The AO is the dominant pattern of winter sea-level pressure fields over north of 20°N with no prefered frequency. In particular, the ENSO index based on equatorial Pacific SSTs contains the variations related to both ENSO and IPO (or PDO), thus we refer it as the ENSO&IPO variability. More details about these climate modes can be found in the cited references.

We used the SST anomalies averaged over the Niño3.4 region (120°W-170°W and 5°S-5°N) as the ENSO&IPO index, which contains both the interannual ENSO and the decadal to multidecadal IPO variations. The monthly AO index was acquired from the Climate Prediction Center (CPC) of NOAA (http://www.cpc.ncep.noaa.gov/products/precip/CWlink/daily_ao_index/history/method.shtml), which was constructed by projecting the monthly 1000-hPa height anomalies onto the leading empirical orthogonal function (EOF) of the 1000-hPa height fields over north of 20^{o}N. The AO index was normalized by the standard deviation of the base period from 1979-2000. The AMO index (unsmoothed and undetrended) used in this study was defined as the North Atlantic monthly SST anomaly averages over 0°-70°N based on the HadISST dataset (Rayner et al., 2003). The global-warming component in all these indices was removed using regression against the time series of historical external anthropogenic forcing as described below.

2.3. Analysis Methods

We applied an EOF analysis to the $NDVI_{gs}$ on the 2.5^{o} grid excluding areas with a mean $NDVI_{gs}$<0.1 and north of 70°N to reveal the leading modes of $NDVI_{gs}$ variability and its possible relation with external forcing during 1982-2013. An EOF analysis of a time series of 2-dimentional fields expresses the data in terms of orthogonal base functions (or spatial patterns), which are determined by the data, and the leading modes often reveal the dominant temporal and spatial patterns in the data. It is similar to performing a principal component analysis, except that the EOF method is often applied to a time series of 2-dimensional fields of the same variable (i.e., taking the time series at each location as a separate variable), instead of the time series of possibly correlated variables.

To quantify the influences from individual climate drivers, we examined the correlations between $NDVI_{gs}$ and local growing-season T, P, sc_PDSI_pm or PAR. The correlation between $NDVI_{gs}$ and annual ENSO&IPO, AMO, and AO indices were also computed to indicate how remote climate oscillations were related to vegetation growth. Additionally, a maximum covariance analysis (MCA, Bretherton et al., 1992) of the $NDVI_{gs}$ and annual SST fields was conducted to investigate the possible teleconnection between terrestrial vegetation activity and oceanic surface conditions. The MCA is similar to EOF decomposition except for extracting the leading modes of the co-variance between two 2-dimentional fields, such as the $NDVI_{gs}$ and SST fields. All these analyses were done with the linear trends removed in order to focus on the relationship of year-to-year variations.

Over the relatively short period from 1982-2013, apparent linear trends in both $NDVI_{gs}$ and the climate drivers can result from either internal decadal-multidecadal variations associated with the ENSO&IPO, AMO, and AO, or external climate forcing such as volcanic eruptions and changes in solar irradiance (external natural forcing), or increases in GHGs and manmade aerosols (external anthropogenic forcing) (see Fig. 8.18 of Myhre et al., 2013). To quantify the contributions from the internal climate variations and externally-forced climate changes to the $NDVI_{gs}$ trends during 1982-2013, we performed a multiple regression analysis as outlined below. Similar regression methods have been used previously (e.g., Dai et al., 2015; Dong and Dai, 2017) and were found to be effective in separating the forced response from internal climate variations. We emphasize that the atmosphere and Earth's surface have a fairly fast response time (in the order of days) to external forcing (such as volcanic eruptions or GHG changes).

Thus for annual-mean response over a large region, the linear regression method without time lags should work reasonably well. Also, because there exists little trend in the external natural forcing during our analysis period from 1982-2013, we only use the external anthropogenic forcing in the trend attribution as described below.

First, we regressed annual time series of ENSO&IPO, AMO, and AO indices onto the external anthropogenic radiative forcing (including GHG and manmade aerosol forcing) over the longer period from 1900-2013 (see Fig. S1 in the Supplementary Information or SI). We then subtracted the regressed part from the raw ENSO&IPO, AMO, and AO indices to remove the externally-forced component. Using AMO as an example, we have

$$AMO_{ex} = a + b \times EF \ , \tag{1}$$

$$AMO_{new} = AMO_{raw} - AMO_{ex} \ , \tag{2}$$

Where AMO_{ex} is the regressed part of the AMO index that is associated with the nonlinear external anthropogenic forcing (see Fig. S1), a and b are the regression coefficients using data from 1900-2013, AMO_{raw} is the raw AMO index, and AMO_{new} is the resdiual (referred to as the detrended AMO index) without the externally-forced component. We attributed the remaining trends in AMO_{new} to internal climate variations. $ENSO\&IPO_{new}$ and AO_{new} were derived by the same procedure as AMO_{new}.

The use of a longer period from 1900-2013 in estimating the regression coefficients a and b is to minimize the aliasing of the forced signal with other internal variations as their correlations are much weaker over 1900-2013 than over shorter periods such as 1982-2013. Here, we implicitly assumed that internal climate variations would not produce a long-term component that resembled the external forcing series with mnotonical increases shown in Fig. S1 over

1900-2013.This assumption is less likely to be valid for shorter periods such as 1982-2013 since multi-decadal oscillations from AMO or IPO can produce changes that are correlated with the forcing series over such short periods.

After removing the component associated with the external anthropogenic forcing, we linearly detrended the $ENSO\&IPO_{new}$, AMO_{new} and AO_{new} indices at each 2.5° grid box to remove the trends from the multiple regression with $NDVI_{gs}$. The detrended values are denoted as $NDVI_{gs}\_d$, $ENSO\&IPO_{new}\_d$, AMO_{new}_d, and AO_{new}_d. In addition, there exists a weak correlation between AMO_{new}_d and AO_{new}_d (r=-0.35) over 1982-2013, and no correlation between $ENSO\&IPO_{new}\_d$ and AMO_{new}_d (r=0.01) or AO_{new}_d (r=-0.04). We assumed that the AMO (an oceanic mode with long memories) is the driving force for this covariance between AMO_{new}_d and AO_{new}_d (an atmospheric mode with short memories). Thus, before performing the following regression, the AMO-correlated part was removed from AO_{new}_d (denoted as AO_{new}_d'). This correlated part was also removed from undetrended AO_{new} using the same regression of AO_{new}_d on AMO_{new}_d, denoted as AO_{new}'. The multiple regression over 1982-2013 has the form:

$$NDVI_{gs}\_d = b0 + b1 \times ENSO\&IPO_{new}\_d + b2 \times AMO_{new}\_d + b3 \times AO_{new}\_d' . \quad (3)$$

Note that the three independent variables in eq. (3) were uncorrelated and the regression coefficients (*b0*, *b1*, *b2* and *b3*) in eq. (3) were derived from interannual to decadal variations during 1982-2013. A key assumption in this study is that the regression coefficients of eq. (3) are also valid for the relationship among long-term changes (i.e., trends) in these variables during 1982-2013. This is reasonable since similar physical processes are behind natural climate variations and long-term (decadal-centennial) climate changes (Dai, 2016). Under this assumption, we used the regression coefficients in eq. (3) and the un-detrended $ENSO\&IPO_{new}$, AMO_{new} and AO_{new}' indices, which contain a linear trend of -0.22, 0.70 and 0.04 per decade during 1982-2013, respectively, to estimate the part of the $NDVI_{gs}$ (referred to as $NDVI_{gs}$_IN) that is attributable to the internal climate changes. The inferred part of the $NDVI_{gs}$ ($NDVI_{gs}$_EX) that is attributable to all external forcing (such as GHG increases and land use changes, Zhu et al. 2016) is obtained by subtracting $NDVI_{gs}$_IN from the raw $NDVI_{gs}$. Thus, we have

$$NDVI_{gs}\_IN = b0 + b1 \times ENSO\&IPO_{new} + b2 \times AMO_{new} + b3 \times AO_{new}', \tag{4}$$

$$NDVI_{gs}\_EX = NDVI_{gs} - NDVI_{gs}\_IN. \tag{5}$$

The linear trends in $NDVI_{gs}$_IN and $NDVI_{gs}$_EX represent the trend parts attributable to internal climate variations and external forcing, respectively. $NDVI_{gs}$_EX includes the effects on vegetation from anthropogenic climate change, CO_2 fertilization, and all other mechanisms. We did not attempt to quantify these individual effects here, but our $NDVI_{gs}$_EX still provides an independent estimate of the externally-forced total $NDVI_{gs}$ change for comparison with model-based estimates (e.g., Los, 2013; Mao et al., 2013, 2016; Zhu et al., 2016). Furthermore, since the trend in the external natural forcing during 1982-2013 is very small, $NDVI_{gs}$_EX is primarily due to the external anthropogenic forcing. Due to the relatively short length of the NDVI record, we did not split it into sub-periods to investigate the effect of the possible change in the vegetation-climate relationship as done by Piao et al. (2014).

3. Results

3.1. Changes and variations in $NDVI_{gs}$ from 1982-2013

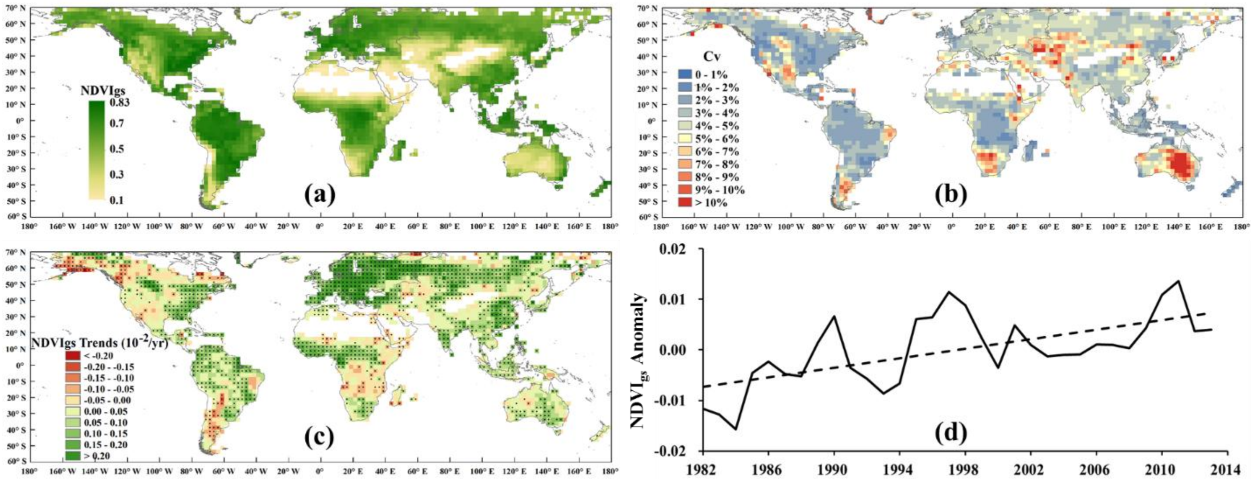

Fig. 1. Maps of (a) the 1982-2013 mean growing-season NDVI ($NDVI_{gs}$). The growing season is defined here as April-October for 20°N-70°N, October-April for 20°S-60°S, and from January-December for 20°S-20°N. Areas with long-term mean $NDVI_{gs}$<0.1 are in blank, (b) coefficient of variation (CV) of $NDVI_{gs}$, defined as the ratio (in %) of the standard deviation to the mean, and (c) linear trends (in change per year) of $NDVI_{gs}$ from 1982 to 2013. Trends significant at the 0.10 level are marked with dots. Also shown (d) is global-mean $NDVI_{gs}$ anomalies (solid line) and its linear trend (dashed line, 0.00474 per decade) from 1982-2013 averaged over all grid cells with long-term mean $NDVI_{gs}$>0.1.

The 1982-2013 mean $NDVI_{gs}$ is shown in Fig. 1a. Areas with a mean $NDVI_{gs}$ < 0.1 are masked as blank. Large $NDVI_{gs}$ values (0.5-0.8) with dense vegetation cover are found over East and Northwest North America, most South America, central Africa, most Europe, and North, East and Southeast Asia. In contrast, Southwest North America, southern South America, southern and northern Africa, central and western Asia, and most Australia have low $NDVI_{gs}$ values (<0.4) with poor vegatation cover. The interannual variations of $NDVI_{gs}$ are depicted by the coefficient of variation (CV, i.e., the ratio of the standard deviation to the mean) in Fig. 1b. The CV shows relatively large variations of $NDVI_{gs}$ over central-eastern Australia, central Asia, parts of northern China, southern and eastern Africa, northeastern Brazil, southern South

America, and central North America.

The linar trends in $NDVI_{gs}$ from 1982-2013 are showed in Fig. 1c. Globally, ~48% of the grid cells show significant (with the attained signficance p<0.1) increasing trends, including Europe, most Asia except its Southwest, eastern and parts of central North America, most South America, southern India, southern Sahel, southern Africa and parts of Australia. Only about 8% of the cells show significant (p<0.1) decreasing trends, mainly over Northwest and Southwest North America, southern South America, and central and eastern Africa (Fig. 1c). Averaged over all grid cells with mean $NDVI_{gs}$ > 0.1, the global-mean $NDVI_{gs}$ (Fig. 1d) shows a significant (p<0.01) upward trend of 0.00474 or 1.2% of the mean per decade during 1982-2013. The increasing rate is more notable before 1997 (trend = 0.01145 or 2.8% per decade, p<0.01) than thereafter (trend = 0.00334 or 0.8% per decade, p=0.20).

An EOF analysis was conducted to decompose the $NDVI_{gs}$ variations into various orthogonal modes, which may help identify the leading temporal and spatial patterns in the NDVI dataset. The two leading EOFs and the associated principal components (PCs) of the $NDVI_{gs}$ are shown in Fig. S2. The first EOF, which explains 28.3% of the total variance, shows spatial patterns broadly comparble to the trend map (Fig. 1c) and its PC is highly correlated with the global-mean $NDVI_{gs}$ (Fig. 1d, r=0.97, p<0.01). Thus the EOF1 captures a large portion of the $NDVI_{gs}$ trend. The PC1 shows a significant upward trend for all areas with positive values in Fig. S2a and it is highly correlated (r=0.79, p<0.01) with the total external radiative forcing (including volcanic, solar and anthoropogenic frocing, red line in Fig. S2b, from Myhre et al., 2013). The declines of PC1 around 1984 and 1993 correspond to the El Chichon (in April 1982) and Mt. Pinatubo (in June 1991) volcanic eruptions, although PC2 (Fig. S2d) also contains these volcanic signals. That is, the EOF method is unable to completely separate the volcanic signal from other modes of variability given the relatively short record for 1982-2013. Nevertheless, Fig. S2 shows that the two volcanic eruptions have caused a temporal decline in vegetation growth over a few years following the eruptions, which is consistent with previous reports (Lucht et al., 2002; Soden et al., 2002). Such an effect on vegetation growth is expected given the impacts of the volcanic eruptions on surface air temperature, precipitatin, evapotranspiration (ET) (Dong and Dai, 2017), and the decline in the growth-rate of atmospheric CO_2 (Bousquet et al., 2000). Although vegetation activity declined following Pinatubo eruption, the global carbon sink was enhanced which was possible due to an enhanced oceanic sink, a retarded heterotrophic respiration driven by cooling and drying of the soil, and reduced biomass buring (Angert et al., 2004).

The PC2 (Fig. S2d, 9.8% of the variance) shows a slight upward (downward) trend for the areas with positive (negative) values in Fig. S2c, of which spatial patterns are similar to the precipitation and ET change patterns induced by anthropogenic forcing (see Fig.7 of Dong and Dai, 2017). This indicates that external forcing may have partly contributed to the trends in $NDVI_{gs}$. The 3rd and 4th EOFs (Fig. S3) explain 7.1% and 6.5% of the variance, respectively, and they seem not reflecting any known physical modes.

3.2.The relations between $NDVI_{gs}$ and local and remote climatic conditions

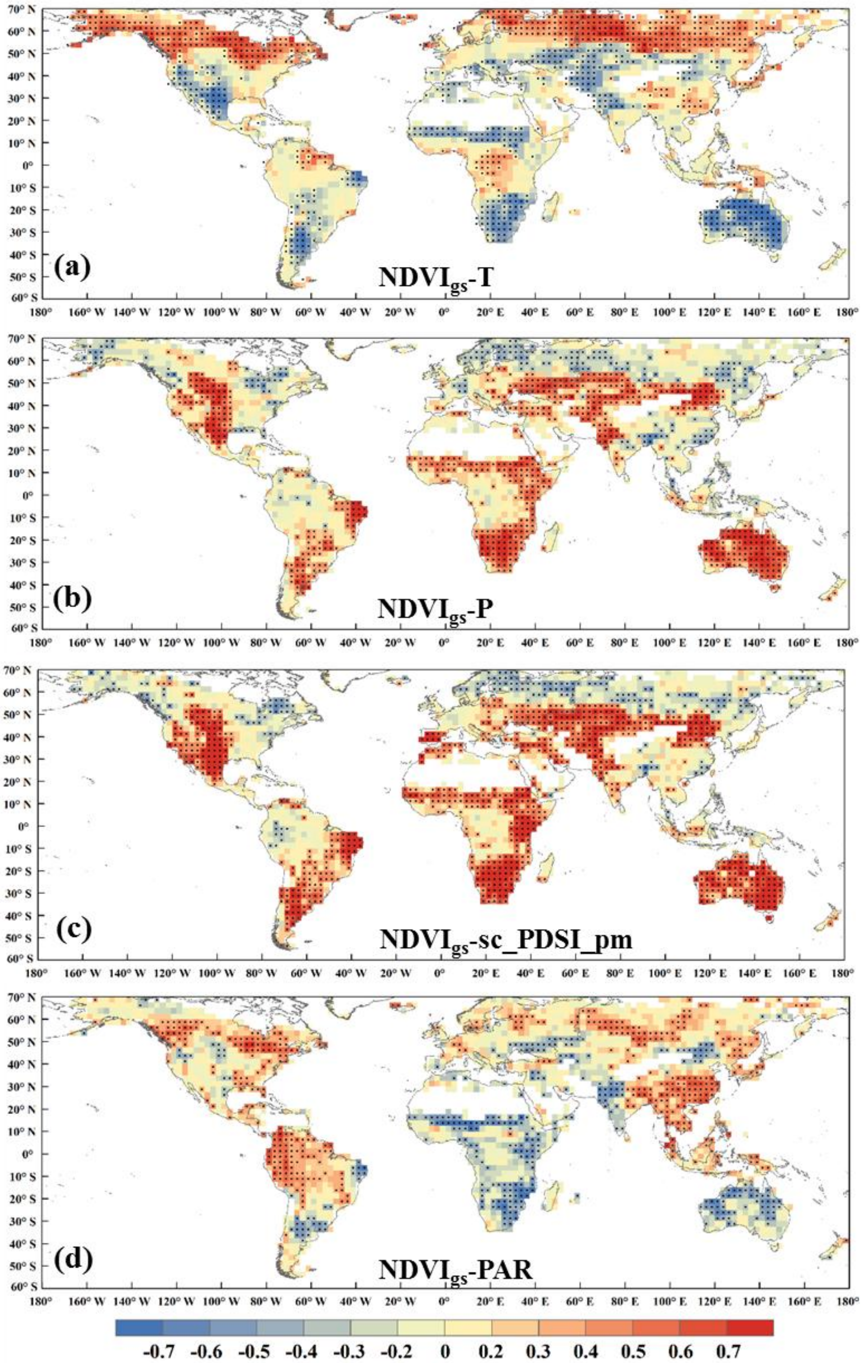

Fig. 2. Maps of correlation coefficients between detrended $NDVI_{gs}$ and detrended (a) surface air temperature (T), (b) precipitation (P), (c) sc_PDSI_pm, and (d) photosynthetically active radiation (PAR) in the growing season during 1982-2013 (1984-2007 for PAR). Correlations significant at the 0.10 level are marked with dots.

Figure 2 shows the correlation coefficients between detrended $NDVI_{gs}$ and T, P, PDSI or PAR during 1982-2013 (1984-2007 for PAR). The correlations measure the coupling strength of the interannual-decadal variations between NDVI and local climate factors. As expected, significant positive correlations between $NDVI_{gs}$ and T are found at northern high latitudes (Fig. 2a), indicating that vegetation growth over these areas is temperature-controlled. $NDVI_{gs}$ is negatively correlated with T over the western U.S., southern South America, the Sahel, southern Africa, central Asia, and Australia. These arid and semi-arid regions also show significant positive correlations between $NDVI_{gs}$ and P and between $NDVI_{gs}$ and sc_PDSI_pm (Fig. 2b-c). This confirms the notion that water is the limiting factor for vegetation growth in arid and semi-arid regions (Nemani et al., 2003), where T arises as the surface dries up, leading to negative $NDVI_{gs}$-T correlations. Figure 2d shows significant positive correlations between $NDVI_{gs}$ and PAR over the Amazon, Southeast Asia and many parts of the middle-latitude NH. This suggests that radiation is also a limiting factor for vegetation growth in those areas.

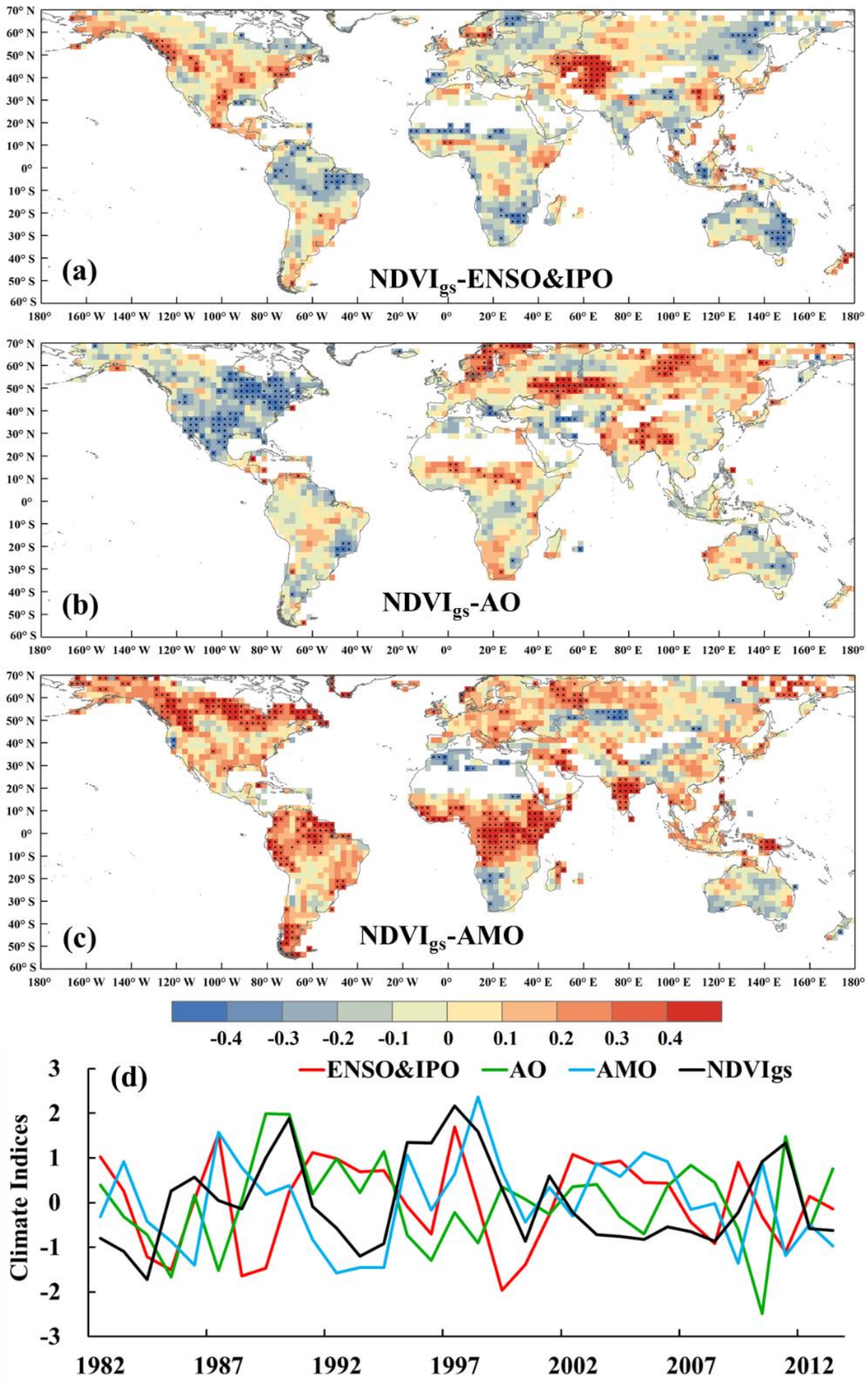

Fig. 3. (a-c) Same as Fig.2 but for the correlation between detrended $NDVI_{gs}$ and detrended annual (a) ENSO&IPO, (b) AO, and (c) AMO index during 1982-2013. (d) Normalized time series of the detrended global-mean $NDVI_{gs}$ (black) and the detrended three oscillation indices. The correlation coefficient between the $NDVI_{gs}$ curve and the index line in (d) is -0.08 for Nino3.4, -0.03 for AO, and 0.29 for AMO.

Figure 3a-c show the correlation maps between detrended $NDVI_{gs}$ and detrended ENSO&IPO, AMO or AO index. It indicates the coupling strength of the interannual-decadal variations between NDVI and remote climate oscillations. $NDVI_{gs}$ is negatively correlated with the ENSO&IPO index over eastern Australia, southern Africa, northeastern South America, and parts of southern and northeastern Asia, suggesting that vegetation growth is suppressed over these regions during El Niño years and IPO warm phases. In contrast, significant positive correlations are seen over southwestern Asia and many parts of North America (Fig.3a). Positive (negative) correlations between $NDVI_{gs}$ and the AO index are seen over most Eurasia (North America) (Fig.3b), indicating that vegetation growth is enhanced (suppressed) over Eurasia (North America) during years with a positive AO phase. Correlations between $NDVI_{gs}$ and the AMO index are mostly postive, especially over northern North America, high-latitude Eurasia, central and eastern Africa, southern India, and most South America (Fig.3c). This suggests that vegetation growth is enhanced over most land areas during postive AMO phases. Globally, $NDVI_{gs}$ is positively correlated with the AMO index ($r=0.29$), while the correlations with the ENSO&IPO ($r=-0.08$) and AO ($r=-0.03$) indices are weak (Fig.3d).

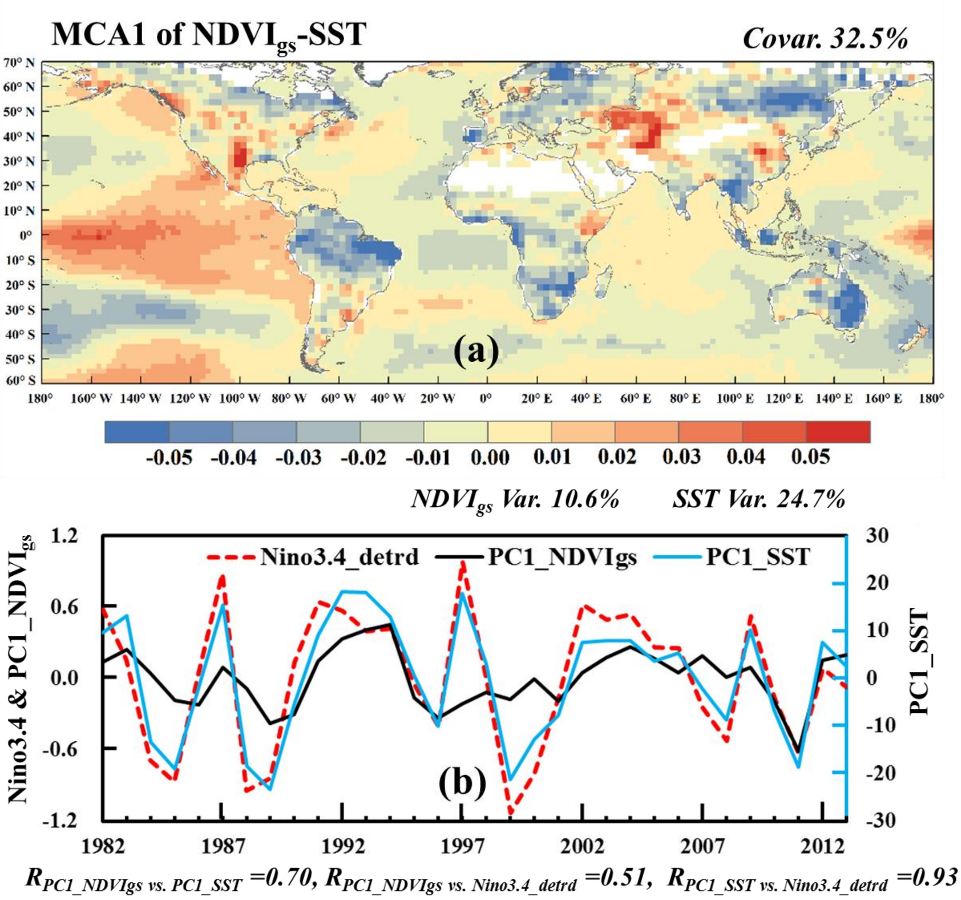

Fig. 4. (a) Spatial patterns and (b) the associated temporal coefficients or PCs (on the right axis for PC1_SST) of the first maximum covariance analysis (MCA) mode for the $NDVI_{gs}$ (land areas) and annual sea surface temperatures (SSTs, ocean areas). The dashed red line in (b) is the detrended Niño3.4 index (on the left axis). The correlations among the lines in (b) are shown below the panel. To indicate the interannual co-variability, both the $NDVI_{gs}$ and SST data were detrended before the MCA analysis.

To further investigate how internal climate modes of variability affect vegetation growth on interannual to decadal time scales through teleconnection, we conducted an MCA analysis of detrended $NDVI_{gs}$ and SST. Figure 4 shows the temporal and spatial patterns of the first MCA mode (MCA1), which explains 32.5% of the covariance and 10.6% and 24.7% of the spatio-temporal variance in the $NDVI_{gs}$ and SST fields, respectively. The PC1 for SST is highly correlated (r=0.93) with the detrended Niño3.4 index while its spatial pattern resembles that of

ENSO&IPO (Fig. 4). Thus, this leading MCA mode is associated with ENSO&IPO. Figure 4 shows that during warm El Niño (cold La Niña) events, vegetation growth is suppressed (enhanced) over tropical South America, most Africa, Australia, midlatitude and South Asia, most Europe, northern Canada and Alaska, but it is enhanced (suppressed) over western Asia, central eastern China, parts of eastern Africa, the central contінguous U.S., and Pacific coasts of Canada and Alaska. While many of these $NDVI_{gs}$ anomaly patterns are consistent with the ENSO-induced precipitation anomalies (e.g., Dai and Wigley 2000), the areas with negative $NDVI_{gs}$ anomaleis are more widespread than those with negative precipitation anomalies, possibly reflecting the additioanl influence of the Niño3.4 SST anomalies on land temperatures (Dong and Dai 2015) and other fields (e.g., cloudiness and thus PAR). These results show that ENSO is the leading internal climate oscillation that can signficantly affect global vegetation growth on interannual to multi-year time scales, confirming findings of many previous studies (e.g., Nicholls, 1991; Mennis, 2001; Nemani et al, 2003; Woodward et al., 2008; Bothale and Katpatal, 2014; Philippon et al., 2014; Erasmi et al., 2014; Miralles et al., 2014).

MCA2 (MCA3) explains 21.6% (10.0%) of the covariance, and 13.9% (4.5%) and 11.8 (13.2)% of the spatio-temporal variance in the $NDVI_{gs}$ and SST fields, respectively (Figs. S4-S5). The PC2 for SST is also correlated (r=-0.73) with the detrended Niño3.4 index. This indicates that the MCA2 mode is partly negatively associated with ENSO&IPO, and the $NDVI_{gs}$ responses are mostly negative (Fig. S4). The MCA3 (Fig. S5) reflects mostly the signal for 1983, 1987 and 1998, with large positive SST anomalies in the tropical eastern Pacific in those years and some negative SST anamolies over the northeastern North Pacific and tropical central Pacific. The $NDVI_{gs}$ response is mostly positive (Fig. S5). Both these MCA modes appear to still reflect some aspects of the ENSO&IPO variability.

3.3.Contribution of internal climate variations and external forcing to NDVI$_{gs}$ trends

To help understand the causes of the recent NDVI$_{gs}$ changes, here we present results from an attribution analysis (see section 2.3) over the globe. The total variance (in %) of the detrended NDVI$_{gs}$ explained by the three internal climate modes is shown in Fig.S6 in SI. Together, these modes explain 15-30% of NDVI$_{gs}$'s variance over most Canada, parts of the central U.S., northern Europe, western Asia, India, eastern Australia, eastern Africa, parts of South and West Africa, and parts of South America. The extra percentage variance explained by the individual climate modes in addition to that explained by the other two modes are shown in Fig. S7. Fig. S6b shows the leading mode that explains the largest NDVI$_{gs}$ variance at each grid. ENSO&IPO has the largest influence on NDVI$_{gs}$ over northeastern Brazil, parts of the Amazon, southern Africa, eastern Australia, southwestern, southern and eastern Asia. AO shows the largest effect over low-latitude North America and northern Eurasia, while AMO has the largest impact over mid-high latitude North America, central and eastern Africa, northern South America, and parts of Eurasia (Fig. S6b).

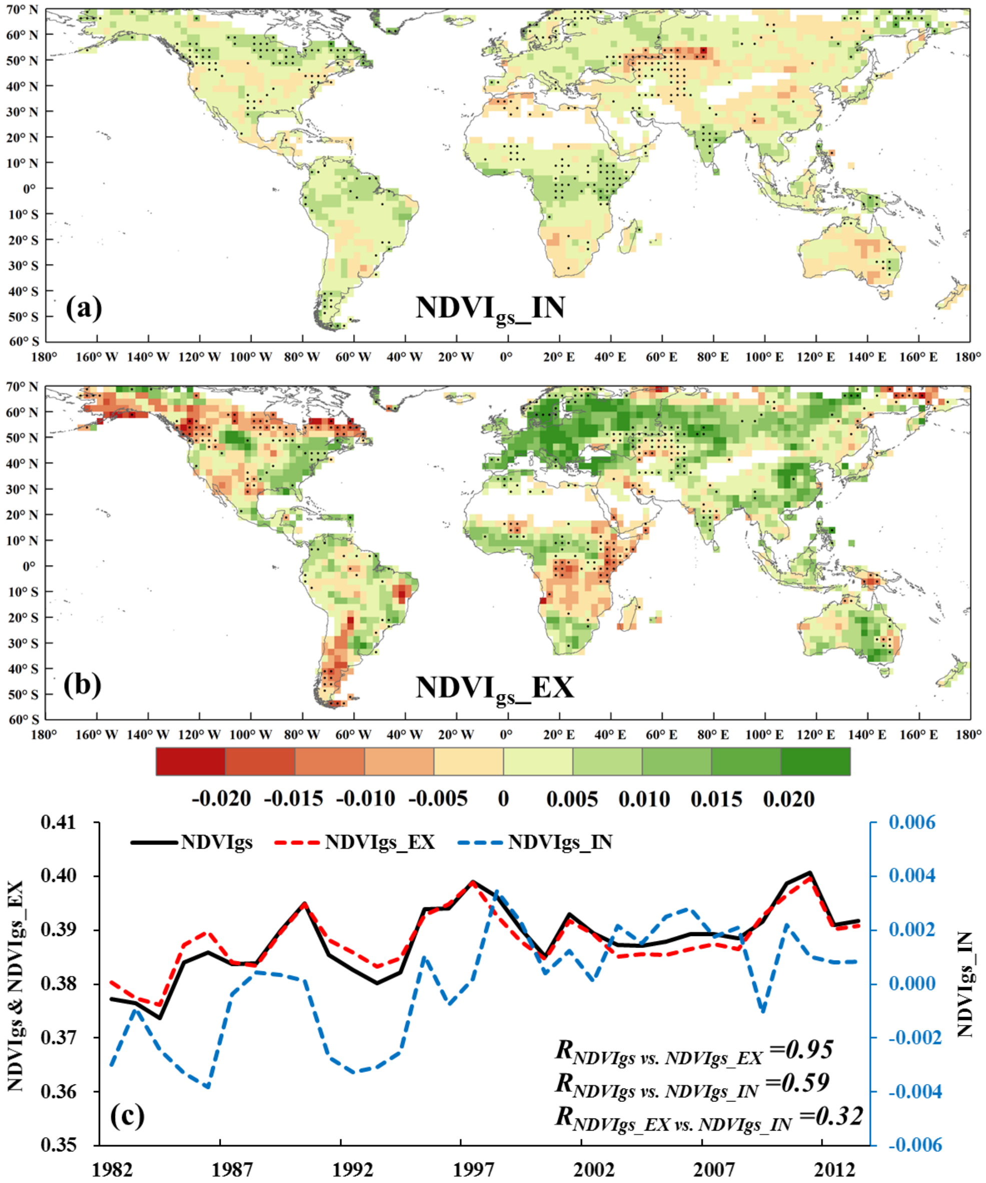

Fig. 5. Maps of $NDVI_{gs}$ trends during 1982-2013 (in units of change per decade) reconstructed using (a) internal climate modes (ENSO&IPO, AMO and AO), (b) inferred $NDVI_{gs}$ trends due to external anthropogenic forcing. (c) Global-mean time series of $NDVI_{gs}$_IN (right axis), $NDVI_{gs}$_EX (left axis), and $NDVI_{gs}$ (left axis) with correlation coefficients among them shown. Areas with the regression using eq. (3) being significant at the 0.10 level are marked with dots in (a) and (b).

Our trend attribution analysis (based on eqs. 4-5) shows that the external forcing is the main contributor to the $NDVI_{gs}$ trend from 1982-2013, while the contribution from the three internal climate modes is relatively small (Fig.5a-b). The internal modes induce some weak greening trends over Canada and Alaska, East and central Africa, and southern South America that offset some of the decreasing trends induced by the external forcing over these regions (Fig.5a-b). In contrast, the internal modes enhance the greening trends induced by the external forcing over central and southern India, Europe, West Africa and northern South America (Fig. 5a-b). The internal modes also induce large $NDVI_{gs}$ decreases over central Asia (Fig. 5a). Globally averaged (Fig.5c), the external foricng (mainly anthropogenic forcing) explains about two thirds (~66%) of the $NDVI_{gs}$ trend, with the remaining (~34%) explained by the three internal modes.

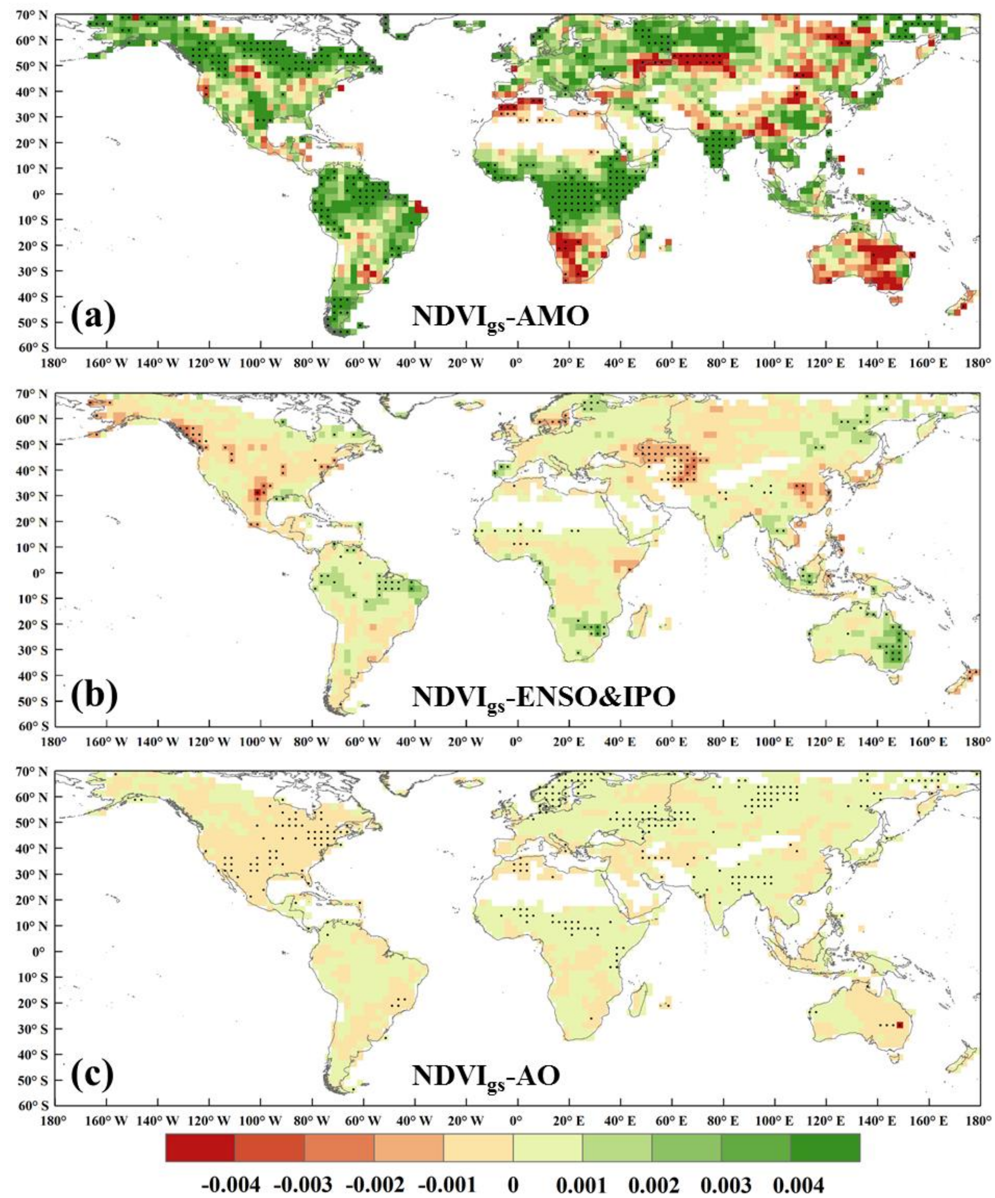

Fig. 6. Maps of the $NDVI_{gs}$ trends from 1982-2013 (in units of change per decade) reconstructed individually using indices for (a) AMO_{new}, (b) $ENSO\&IPO_{new}$, and (c) AO_{new}. Dots indicate the regression coefficient is significant at the 0.10 level in eq. (3). As these maps were calculated based on the regression coefficients (*b1*, *b2*, *b3*) of Eq. (3), the significance level of the mapped data depends on that of regression coefficients (though in part depends on significance of trends in climate indices).

Figure 6 shows the maps of the $NDVI_{gs}$ trends reconstructed using the three individual climatic modes. The AMO, which has a relatively large trend after removing the component associated with historical external anthropogenic forcing (Table S1 in SI), contributes the most to the $NDVI_{gs}$ trends over high-latitude North America and Eurasia, South America, most Africa, Australia, and India. The spatial pattern of the AMO contribution (Fig.6a) is generally consistent with previous studies which have shown that warm phase of AMO would lead to reduced precipitation and high temperatures over North America (Enfield et al., 2001; Schubert et al., 2009), warming over most East Asia (Wang et al., 2009), increased precipitation over India (Li et al., 2008) and West Africa (Zhang et al., 2006), reduced rainfall over Northeast Brazil (Knight et al., 2006) and increased summer rainfall and temperature over West Europe (Sutton and Hodson, 2005). These variations in precipitation and temperature would lead to corresponding changes in $NDVI_{gs}$ based on the correlatins shown in Fig. 3a-b.

The contributions from the ENSO&IPO to $NDVI_{gs}$ trends are small (Fig.6b), with some negative trends over parts of central Asia, western Canada, and central China, and positive trends over Northeast Brazil, southern Africa, eastern Australia, southern Asia, and Northwest Pacific. The attribution of AO to $NDVI_{gs}$ trends is negligible (Fig.6c). The small trend contributions from ENSO&IPO and AO are possibly due to the small trends in these indices after removing the component associated with the long-term external anthropogenic forcing and that associated with the AMO (for AO case) (Table S1 and Fig. S8). For ENSO&IPO, the relatively short period from 1982 to 2013 includes an upward phase and a downward phase, resulting in a small trend (Fig. S1c). For AO (Fig. S1b), its small trend during 1982-2013 is correlated with AMO and thus is attributed to the latter, as explained in section 2.3. This results in a very small trend contribution from AO. In contrast, the increase of the AMO index after ~1972 leads to a significant increasing trend for the AMO index during 1982-2013 (Fig. S1a and

Table S1).

4. Summary and Discussion

In this study, we have investigated the spatio-temporal variations of $NDVI_{gs}$ over the global (60^oS-70^oN) land during 1982-2013 using EOF decomposition, examined their relations to local climate factors and remote climate oscillations using correlation and MCA analyses, and estimated the contributions by external forcing and internal climate variations to observed $NDVI_{gs}$ trends using regression analyses.

Results show a greening trend from 1982-2013 over Eurasia, eastern North America, southeastern Asia, northern South America, Sahel, and Australia, and browning over southern Africa, southern South America and northern North America (Fig.1c). Globally averaged, there was a significant upward trend in $NDVI_{gs}$ (~0.00474 units per decade) from 1982-2013, especially before 1997 (Fig.1d). The NDVI trend patterns shown here are consistent with those reported in previous studies (e.g., Xiao and Moody, 2005; De Jong et al., 2012; Ukkola et al., 2015; Julien et al., 2006). The two pronounced declines of global $NDVI_{gs}$ around 1984 and 1993 (Fig.1d) are likely caused by the cooling effect after two volcanic erruptions in 1982 and 1991 (Lucht et al., 2002; Soden et al., 2002).

As expected, $NDVI_{gs}$ is found to be temperature-limited over the high-latitude Northern Hemisphere, but water-limited in arid and semi-arid regions, and radiation-limited over the Amazon, eastern and southearn Asia, and parts of the middle-latitude Northern Hemisphere (Fig.2), which are in agreement with previous results (e.g., Nemani et al., 2003; Piao et al., 2014). The MCA analysis shows that ENSO is the leading climate oscillation that affects interannual variability of global vegetation growth (Fig.4), with warm ENSO&IPO events leading to vegetation decline over southern Africa, Australia, India, northern South America, northeastern and southern Asia, while the opposite occurs over North America, central Asia, eastern Africa and eastern China (Figs.3-4), which are in agreement with many previous studies (eg., Woodward et al., 2008; Miralles et al., 2014; Bothale and Katpatal, 2014). A North America-Eurasia dipole pattern in the $NDVI_{gs}$-AO correlation (Fig.3b) is expected given the influence of AO to NH climate and greenness (Thompson and Wallace, 1998; Buermann et al., 2003). Significant correlations between interannual to decadal variablity of NDVI and AMO are found over large land areas (Fig.3c), indicating that AMO is a global climate mode that shoud not be ignored and probably influence not only the Atlantic-surrounded areas but also areas away from the Atlantic, such as the western tropical Pacific (Sun et al., 2017).

Based on the observational data and regression analysis, our study attributes about two thirds (~66%) of the global growing-season NDVI trend to the external anthropogenic forcing during 1982-2013, while the internal climate variations account for the rest (~34%) (Fig.5). Our attribution results are consistent with the modelling study of Mao et al. (2016), who showed that the external anthropogenic forcings (mainly GHGs) contribute the most to the greening trends over northern extratropical land. However, there are differences in the estimated contributions between this study and other previous modelling studies (e.g., Los, 2013; Mao et al., 2013; Zhu et al., 2016), which have attributed the global greening trends to CO_2 fertilization, climate change, nitrogen depostion, and other factors. The possible explanation is that these previous studies separated the CO_2 fertilization effect from its climatic effect while in our study they are combined together, including the impact of other GHGs and manmade aerosols besides CO_2.

Furthermore, due to modeling uncertainties and different attribution analysis methods, there are large discrepancies among the previous results. For example, CO_2 fertilization is considered as the dominant driving factor by Mao et al. (2013), and it accounts for 40% of the greening trend in Los (2013) and 70% in Zhu et al. (2016); while climate change accouts for 40% in Los (2013) and 8% in Zhu et al. (2016). In addition, there are interactions among climate change, CO_2 fertilization and nitrogen deposition (Piao et al., 2015), which are not fully taken into account in ecosystem modeling.

Here, we further quantified the relative contribution from internal climate variablity in addition to the contribution by the anthropogenic forcing, and we tried to further separate the contribution from internal climate variability into three climae modes (ENSO&IPO, AMO, and AO). It is suggested that AMO contributes the most to the $NDVI_{gs}$ trend among the three climate modes examined here (Fig.6). This is due to the relatively large trend in the AMO index but small trends in the other two indices after removing the component associated with the long-term anthropogenic forcing series (Table S1). The global widespread influence of AMO on vegetation (Fig.3c) is another possible explanation. The spatial patterns of the AMO-induced $NDVI_{gs}$ trends are expected given the $NDVI_{gs}$-AMO correlation (Fig.3c), $NDVI_{gs}$-T and $NDVI_{gs}$-P relationship (Fig.2a-b), and the reported climate impacts of AMO (eg., Knight et al., 2006). This result emphasizes the important role of AMO on vegetaiton over globe (Bastos et al., 2017).

Overall, our study suggests that the interannual variablity of global NDVI in recent decades is dominated by variations induced by ENSO, and the global greening trends are primarily attributable to external anthropogenic forcing (~66%, mainly GHGs), with the rest explained by internal climate modes (mainly AMO). Although our attribution results likely depend on the regression method used in our analysis, they are derived from an approach different from previous modeling studies, which can provide an estimate independent of the modeling studies.

Acknowledgements

A. Dai acknowledges the funding support from the U.S. National Science Foundation (Grant #AGS-1353740), U.S. Department of Energy's Office of Science (Award #DE-SC0012602), and U.S. National Oceanic and Atmospheric Administration (Award #NA15OAR4310086). This study is also supported by National Natural Science Foundation of China (Grant #41301586) and China Postdoctoral Science Foundation (Grants #2014T70731). This work was conducted during a visit by L. Zhao to the University at Albany supported by the China Scholarship Council (CSC).

References

Angert, A., Biraud, S., Bonfils, C., Buermann, W., Fung, I., 2004. CO_2 seasonality indicates origins of post‐Pinatubo sink. Geophys. Res. Lett. 31, 293-317

Anyamba, A., Tucker, C.J., 2005. Analysis of Sahelian vegetation dynamics using NOAA AVHRR NDVI data from 1981–2003. J. Arid Environ. 63, 596-614.

Bastos, A., Ciais, P., Park, T., et al., 2017. Was the extreme Northern Hemisphere greening in 2015 predictable? Environ. Res. Lett., 12, doi: 10.1088/1748-9326/10/aa67b5.

Bothale, R.V., Katpatal, Y.B., 2014. Response of rainfall and vegetation to ENSO events during 2001–2011 in upper Wardha watershed, Maharashtra, India. J. Hydrol. Eng. 19, 3, 583-592.

Bousquet, P., Peylin, P., Ciais, P., Le Quere, C., Friedlingstein, P., Tans, P.P., 2000. Regional changes in carbon dioxide fluxes of land and oceans since 1980. Science, 290, 1342-1346.

Bretherton, C.S., Smith, C., Wallace, J.M., 1992. An intercomparison of methods for finding coupled patterns in climate data. J. Climate 5, 541–560.

Buermann, W., Anderson, B., Tucker, C.J., et al., 2003. Interannual covariability in Northern Hemisphere air temperatures and greenness associated with El Niño-Southern Oscillation and the Arctic Oscillation. J. Geophys. Res. 108, D13, 4396, doi: 10.1029/2002JD002630.

Ciais, P., Reichstein, M., Viovy, N., et al., 2005. Europe-wide reduction in primary productivity caused by the heat and drought in 2003. Nature, 437, 529-533.

Churkina, G., Running, S.W., 1998. Contrasting climatic controls on the estimated productivity of global terrestrial biomes. Ecosystems, 1998, 1, 206-215.

Dai, A., Trenberth, K.E., Qian, T., 2004. A global data set of Palmer Drought Severity Index for 1870-2002: Relationship with soil moisture and effects of surface warming. J. Hydrometeorol. 5, 1117-1130.

Dai, A., 2011a. Characteristics and trends in various forms of the Palmer Drought Severity Index (PDSI) during 1900-2008. J. Geophys. Res. 116, D12115. doi: 10.1029/2010JD015541.

Dai, A., 2011b. Drought under global warming: A review. WIRES Clim. Change, 2, 45-65.

Dai, A., 2013. Increasing drought under global warming in observations and models. Nat. Clim. Change, 3, 52-58.

Dai, A., 2016. Future warming patterns linked to today's climate variability. Sci. Rep. 6, 19110, doi: 10.1038/srep19110.

Dai, A., Fung, I.Y., 1993. Can climate variability contribute to the "missing" CO_2 sink? Global

Biogeochem. Cy. 7, 599-609.

Dai, A., Wigley, T.M.L., 2000. Global patterns of ENSO-induced precipitation. Geophys. Res. Lett. **27**, 1283–1286. doi: 10.1029/1999GL011140.

Dai, A., Zhao, T., 2017. Uncertainties in historical changes and future projections of drought. Part I: Estimates of historical drought changes. Climatic Change, **144**, 519-533. DOI: 10.1007/s10584-016-1705-2.

De Jong, R., Verbesselt, J., Schaepman, M.E., De Bruin, S., 2012. Trend changes in global greening and browning: contribution of short-term trends to longer-term change. Global Change Biol. **18**, 642-655.

De Jong, R., Schaepman, M.E., Furrer, R., Bruin, S., Verburg, P.H., 2013. Spatial relationship between climatologies and changes in global vegetation activity. Global Change Biol. 19, 1953–1964.

Dong, B., Dai, A., 2015. The influence of the Interdecadal Pacific Oscillation on temperature and precipitation over the Globe. Clim. Dynam. 45, 2667-2681.

Dong, B., Dai, A., 2017. The uncertainties and causes of the recent changes in global evapotranspiration from 1982-2010. Clim. Dynam. 49: 279-296.

Doughty, C.E., Metcalfe, D.B., Girardin, C.A.J., et al., 2015. Drought impact on forest carbon dynamics and fluxes in Amazonia. Nature, 519, 78-82.

Enfield, D.B., Mestas-Nuñez, A.M., Trimble, P.J., 2001. The Atlantic Multidecadal Oscillation and its relation to rainfall and river flows in the continental U.S. Geophys. Res. Lett. 28, 2077-2080.

Erasmi, S., Schucknecht, A., Barbosa, M.P., Matschullat, J., 2014. Vegetation greenness in northeastern Brazil and its relation to ENSO warm events. Remote Sens. 6, 3041-3058.

Fensholt, R., Langanke, T., Rasmussen, K., et al., 2012. Greenness in semi-arid areas across the globe 1981-2007—an earth observing satellite based analysis of trends and drivers. Remote Sens. Environ. 121, 144-158.

Gu, G., Adler, R.F., 2013. Interdecadal variability/long-term changes in global precipitation patterns during the past three decades: global warming and/or pacific decadal variability? Clim. Dynam. 40, 3009-3022.

Gu G., Adler, R.F., 2015. Spatial patterns of global precipitation change and variability during 1901-2010. J. Clim. 28, 4431-4453.

Harris, I., Jones, P., Osborn, T., Lister, D., 2014. Updated high-resolution grids of monthly climatic observations-the CRU TS3. 10 Dataset. Int. J. Climatol. 34, 623–642.

Hickler, T., Eklundh, L., Seaquist, J.W., et al., 2005. Precipitation controls Sahel greening trend. Geophys. Res. Lett. 32, L21415. doi: 10.1029/2005GL024370.

Huffman, G.J., Adler, R.F., Bolvin, D.T., Gu, G., 2009. Improving the global precipitation record: GPCP Version 2.1. Geophys. Res. Lett. 36, L17808. doi: 10.1029/2009GL040000.

Ichii, K., Kawabata, A., Yamaguchi, Y., 2002. Global correlation analysis for NDVI and climatic variables and NDVI trends: 1982-1990. Int. J. Remote Sens. 23, 3873-3878.

Ji, L., Peters, A.J., 2003. Assessing vegetation response to drought in the northern Great Plains using vegetation and drought indices. Remote Sens. Environ. 87, 85-98.

Julien, Y., Sobrino, J.A., Verhoef, W., 2006. Changes in land surface temperatures and NDVI values over Europe between 1982 and 1999. Remote Sens. Environ. 103, 43-55.

Kawabata, A., Ichii, K., Yamaguchi, Y., 2001. Global monitoring of interannual changes in vegetation activities using NDVI and its relationships to temperature and precipitation. Int. J. Remote Sens. 22, 1377-1382.

Knight, J.R., Folland, C.K., Scaife, A.A., 2006. Climate impacts of the Atlantic Multidecadal Oscillation. Geophys. Res. Lett. 33, doi: 1011029/2006GL026242.

Li, S., Perlwitz, J., Quan, X., Hoerling, M.P., 2008. Modelling the influence of North Atlantic multidecadal warmth on the Indian summer rainfall. Geophys. Res. Lett. 2008, 35, L05804, doi: 10.1029/2007GL032901.

Liu, Z., 2012. Dynamics of interdecadal climate variability: a historical perspective. J. Climate, 25, 1963–1995.

Los, S.O., 2013. Analysis of trends in fused AVHRR and MODIS NDVI data for 1982–2006: Indication for a CO_2 fertilization effect in global vegetation. Global Biogeochem. Cy. 27, 318–330.

Lucht, W., Prentice, I.C., Myneni, R.B., et al., 2002. Climatic control of the high-latitude vegetation greening trend and Pinatubo effect. Science, 296, 1687–1689.

Mao, J.F., Shi, X.Y., Thornton, P.E., Hoffman, F.M., Zhu, Z.C., Myneni, R.B., 2013. Global Latitudinal-Asymmetric Vegetation Growth Trends and Their Driving Mechanisms: 1982–2009. Remote Sens. 5, 1484-1497.

Mao, J.F., Ribes, A., Yan, B.Y., et al., 2016. Human-induced greening of the northern extratropical land surface. Nat. Clim. Change, doi: 10.1038/nclimate3056.

Mennis, J., 2001. Exploring relationships between ENSO and vegetation vigour in the south-east USA using AVHRR data. Int. J. Remote Sens. 22, 3077-3092.

Miralles, D.G., van den Berg, M.J., Gash, J.H., et al., 2014. El Niño-La Niña cycle and recent trends in continental evaporation. Nat. Clim. Change, 4, 122-126.

Mitchell, T.D., Jones, P.D., 2005. An improved method of constructing a database of monthly climate observations and associated high-resolution grids. Int. J. Climatol., 25, 693–712.

Myhre, G., Shindell, D., Bréon, F.M., et al., 2013. Anthropogenic and Natural Radiative Forcing. In: Climate Change 2013: The Physical Science Basis. Contribution of Working Group I to the Fifth Assessment Report of the Intergovernmental Panel on Climate Change (eds Stocker, T.F., Qin, D., Plattner, G.K., Tignor, M., Allen, S.K., Boschung, J., Nauels, A., Xia, Y., Bex, V., Midgley, P.M.), PP. 695-782. Cambridge University Press, Cambridge.

Nemani, R.R., Keeling, C.D., Hashimoto, H., et al., 2003. Climate-driven increases in global terrestrial net primary production from 1982 to 1999. Science, 300, 1560-1563.

Nicholls, N., 1991. The El Niño/Southern Oscillation and Australian vegetation. Vegetatio, 91, 23-36.

Olsson, L., Eklundh, L., Ardö, J., 2005. A recent greening of the Sahel—trends, patterns and potential causes. J. Arid Environ. 63, 556-566.

Pasho, E., Camarero, J.J., de Luis, M., Vicente-Serrano, S.M., 2011. Impacts of drought at different time scales on forest growth across a wide climatic gradient in north-eastern Spain. Agr. Forest Meteorol. 151, 1800-1811.

Peng, S., Chen, A., Xu, L., et al., 2011. Recent change of vegetation growth trend in China. Environ. Res. Lett. 6, 044027. doi: 10.1088/1748-9326/6/4/044027.

Philippon, N., Martiny, N., Camberlin, P., Hoffman, M.T., Gond, V., 2014. Timing and patterns of the ENSO signal in Africa over the last 30 years: insights from Normalized Difference Vegetation Index data. J. Climate, 27, 2509-2532.

Phillips, O.L., Aragão, L.E.O.C., Lewis, S.L., et al., 2009. Drought sensitivity of the Amazon rainforest. Science, 323, 1344-1347.

Piao, S., Wang, X., Ciais, P., Zhu, B., Wang, T., Liu, J., 2011. Changes in satellite-derived vegetation growth trend in temperate and boreal Eurasia from 1982 to 2006. Global Change Biol. 17, 3228-3239.

Piao, S., Nan, H., Huntingford, C., et al., 2014. Evidence for a weakening relationship between interannual temperature variability and northern vegetation activity. Nat. commun. 5. doi: 10.1038/ncomms6018.

Piao, S., Yin, G., Tan, J., et al., 2015. Detection and attribution of vegetation greening trend in China over the last 30 years. Global Change Biol. 21, 1601–1609, doi: 10.1111/gcb.12795.

Quiring, S.M., Ganesh, S., 2010. Evaluating the utility of the Vegetation Condition Index (VCI) for monitoring meteorological drought in Texas. Agr. Forest Meteorol. 150, 330-339.

Rayner, N.A., Parker, D.E., Horton, E.B., et al., 2003. Global analyses of sea surface temperature, sea ice, and night marine air temperature since the late nineteenth century. J. Geophys. Res. 108. doi: 10.1029/2002JD002670.

Ropelewski, C.F., Halpert, M.S., 1989. Precipitation patterns associated with the high index phase of the Southern Oscillation. J. Climate, 2, 268-284.

Rossow, W.B., Schiffer, R.A., 1999. Advances in understanding clouds from ISCCP. B. Am. Meteorol. Soc. 80, 2261–2287.

Schimel, D.S., House, J.I., Hibbard, K.A., et al., 2001. Recent patterns and mechanisms of carbon exchange by terrestrial ecosystems. Nature, 414, 169–172.

Schneider, U., Becker, A., Finger, P., Meyer-Christoffer, A., Ziese, M., Rudolf, B., 2014. GPCC's new land surface precipitation climatology based on quality-controlled in situ data and its role in quantifying the global water cycle. Theor. Appl. Climatol. 115, 15-40.

Schubert, S., Gutzler, D., Wang, H., et al., 2009. A U.S. CLIVAR Project to Assess and Compare the Responses of Global Climate Models to Drought-Related SST Forcing Patterns: Overview and Results. J. Climate, 19, 5251-5272.

Schuur, E.A.G., 2003. Productivity and global climate revisited: the sensitivity of tropical forest growth to precipitation. Ecology, 84, 1165-1170.

Soden, B.J., Wetherald, R.T., Stenchikov, G.L., Robock, A., 2002. Global cooling after the eruption of Mount Pinatubo: a test of climate feedback by water vapor. Science, 296, 727-730.

Sun, C., Kucharski, F., Li, J., et al., 2017. Western tropical Pacific multidecadal variability forced by the Atlantic multidecadal oscillation. Nat. Commun., 8, doi: 10.1038/ncomms15998.

Sutton, R.T., Hodson, D.L.R., 2005. Atlantic Ocean forcing of North American and European summer climate. Science, 309, 115-118.

Thompson, D.J.W., Wallace, J.M., 1998. The Arctic Oscillation signature in wintertime geopotential height and temperature fields. Geophys. Res. Lett. 25, 1297-1300.

Trenberth, K.E., Dai, A., van der Schrier, G., Jones, P.D., Barichivich, J., Briffa, K.R., Sheffield, J., 2014. Global warming and changes in drought. Nat. Clim. Change, 4, 17-22.

Tucker, C.J., Pinzona, J.E., Brown, M.E., et al., 2005. An extended AVHRR 8-km NDVI dataset compatible with MODIS and SPOT vegetation NDVI data. Int. J. Remote Sens. 26, 4485-4498.

Ukkola, A.M., Prentice, I.C., Keenan, T.F., van Dijk, A.I.J.M., Viney, N.R., Myneni, R.B., Bi, J., 2015. Reduced streamflow in water-stressed climates consistent with CO_2 effects on vegetation. Nat. Clim. Change, doi: 10.1038/NCLIMATE2831.

Vicente-Serrano, S.M., Gouveia, C., Camarero, J.J., et al., 2013. Response of vegetation to drought time-scales across global land biomes. P. Natl. Acad. Sci. 110, 52-57.

Wang, Y., Li, S., Luo, D., 2009. Seasonal response of Asian monsoonal climate to the Atlantic Multidecadal Oscillation. J. Geophys. Res. 114, doi: 1011029/2008JD010929.

Woodward, F.I., Lomas, M.R., Quaife, T., 2008. Global responses of terrestrial productivity to contemporary climatic oscillations. Philos. T. R. Soc. B: Biol. Sci. 363, 2779-2785.

Xiao, J., Moody, A., 2005. Geographical distribution of global greening trends and their climatic correlates: 1982–1998. Int. J. Remote Sens. 26, 2371-2390.

Xu, G., Zhang, H.F., Chen, B., et al., 2014. Changes in vegetation growth dynamics and relations with climate over China’s Landmass from 1982 to 2011. Remote Sens. 6, 3263-3283.

Zhang, Y., Wallace, J.M., Battisti, D.S., 1997. ENSO-like interdecadal variability: 1900–1993. J. Climate, 10:1004–1020.

Zhang, R., Delworth, T.L., 2006. Impact of Atlantic multidecadal oscillations on India /Sahel rainfall and Atlantic hurricanes. Geophys. Res. Lett. 33, doi: 1011029/2006GL026267.

Zhang, Y., Zhu, Z., Liu, Z., et al., 2016. Seasonal and interannual changes in vegetation activity of tropical forests in Southeast Asia. Agr. Forest Meteorol. 224, 1–10.

Zhao, M., Running, S.W., 2010. Drought-induced reduction in global terrestrial net primary production from 2000 through 2009. Science, 329, 940–943.

Zhou, L., Tucker, C.J., Kaufmann, R.K., Slayback, D., Shabanov, N.V., Myneni, R.B., 2001. Variations in northern vegetation activity inferred from satellite data of vegetation index during 1981 to 1999. J. Geophys. Res. 106, 20269–20283.

Zhou, L., Tian, Y., Myneni, R.B., et al., 2014. Widespread decline of Congo rainforest greenness in the past decade. Nature, 509, 86-90.

Zhu, Z., Piao, S., Myneni, R.B., et al., 2016. Greening of the Earth and its drivers. Nat. Clim. Change, doi: 10.1038/nclimate3004.